Solar RRL
www.solar-rrl.com

Efficient Perovskite Solar Cells Based on Dopant-Free Spiro-OMeTAD Processed With Halogen-Free Green Solvent

Kui Jiang, Fei Wu, Guangye Zhang, Linna Zhu,* and He Yan**

In this paper, highly efficient (17%) perovskite solar cells (PSCs) based on a hole-transporting layer (HTL) made of dopant-free Spiro-OMeTAD processed from a non-halogenated solvent (THF) are reported for the first time. In addition to the high efficiency, a negligible hysteresis effect is observed for the devices with dopant-free Spiro-OMeTAD hole-transporting material (HTM), which is often a problem for planar n-i-p type PSCs. By eliminating the hydroscopic dopants, the ambient stability of the completed PSC devices are much improved. Another advantage of using THF as a solvent is that much less of the Spiro-OMeTAD material is required (5 mg ml^{-1}) to coat the HTL compared to that used in a conventional chlorobenzene solvent (70 mg ml^{-1}). Our result provides a simple yet effective method to fabricate dopant-free PSCs toward cost-effective and environmental friendly production of PSCs with enhanced stability.

Tremendous achievements have been gained in the organic-inorganic hybrid perovskite solar cells (PSCs), since the pioneering work of Miyasaka et al. in 2009, in which the methylammonium lead iodide ($MAPbI_3$) was first introduced as a light absorber.[1–4] With the collaborative developments in processing strategies, materials evolution, interface engineering, and optimization of the device architectures, nowadays the power conversion efficiency (PCE) of PSCs has exceeded 23%, approaching the outstanding performance of traditional silicon solar cells.[5–7] Currently, the most widely studied PSC device is based on the n-i-p structure, also known as the conventional PSCs, wherein the perovskite absorber is sandwiched between two charge selective contacts, that are, a top hole transporting layer (HTL) and a bottom electron-transporting layer (ETL).

Among all state-of-the-art hole-transporting material (HTM) in n-i-p devices, Spiro-OMeTAD (2,2,7,7-tetrakis(*N*,*N*-di-*p*-methoxyphenylamine)9,9-spirobifluorene) is the most representative one to date. Using Spiro-OMeTAD (denoted as Spiro in the context for simplification) as the HTM, PSCs have achieved high efficiencies in the range of 19–22%,[8–9] provided that suitable dopants (Li-TFSI, *t*BP, cobalt dopant FK9209, et al.) are indispensable to enhance the hole mobility and conductivity of Spiro.[10–11] However, a serious concern about the dopants introduced in HTMs lies in the fact that the dopants are usually highly hygroscopic, which easily leads to the degradation of the perovskite material and ultimately deteriorates the device stability.[12–15] In addition, some researches have pointed out that the added dopants tend to form the recombination centers and thus are detrimental to the open-circuit voltage (V_{oc}) of the device.[16–17] Without the addition of dopants in Spiro, however, PSCs could only realize low efficiencies. For example, conventional PSCs using dopant-free Spiro as the HTM typically acquire PCEs lower than 10%.[15,18–19] The inferior performance of pristine Spiro mainly comes from its poor hole mobility because the Spiro thin film prepared from chlorobenzene is typically considered amorphous.[20–22] So far, the highest efficiency of n-i-p PSCs based on undoped Spiro is only about 13.2%, far from the efficiency achieved in devices adopting the doped Spiro.[23]

Here, we report the use of a dopant-free Spiro as the HTM to construct conventional PSCs with an architecture of ITO/C_{60}/perovskite ($MAPbI_{3-x}Cl_x$)/dopant-free Spiro/MoO_3/Ag, which yielded a high efficiency of 17%. The main reason why dopant-free Spiro can work efficiently in our work is the preparation method and the enhanced crystallinity of the film. Instead of processing the Spiro film from chlorobenzene, in this work, we process Spiro from a green solvent, THF, via a dynamic spin-coating approach. Compared to the commonly used solvent chlorobenzene (CB),[24–25] the Spiro films prepared from THF by dynamic spin-coating show an enhanced crystallinity and a higher hole mobility, which is an important reason why dopant-free Spiro can work well. The enhanced crystallinity of Spiro processed by THF was also supported by GIWAXS (grazing-incidence wide-angle X-ray scattering) data. In addition, PSCs based on our dopant-free Spiro achieve a high efficiency of 16.94% from forward scanning and 16.54% from reverse scanning, with negligible hysteresis effect in this type of devices. In addition to the high PCE, the corresponding devices also show

Dr. F. Wu, Prof. L. Zhu
Chongqing Key Laboratory for Advanced Materials and Technologies of Clean Energy, Faculty of Materials & Energy
Southwest University
Chongqing 400715, P.R. China
E-mail: feiwu610@swu.edu; cn; lnzhu@swu.edu.cn

Dr. K. Jiang, Dr. G. Zhang, Prof. H. Yan
Department of Chemistry and Energy Institute
The Hong Kong University of Science and Technology
Clear Water Bay, Hong Kong
E-mail: hyan@ust.hk

DOI: 10.1002/solr.201900061

favorable stability as the dopants in conventional Spiro HTL can cause stability issues.

Generally, the electron-transporting material adopted by the majority of conventional PSCs is TiO_2, which is used as a thin compact layer in planar devices, or together with an additional mesoporous layer of TiO_2 in mesostructured devices. Excellent performances have been achieved in TiO_2-based planar PSCs.[6,26] However, the high PCEs in TiO_2-based PSCs are typically accompanied by serious hysteresis effects.[27] To address this issue, other n-type contacts were developed, such as C_{60} and C_{60} self-assembled monolayers (SAMs).[28–29] The device structure utilized in this work is depicted in **Scheme 1**, wherein evaporated C_{60} was used as the electron transporting layer, the Spiro without any dopants was used as the hole transporting material, and a thin layer of molybdenum oxide (MoO_3) (10 nm) was employed as the buffer layer.[29–30] Spiro was dissolved in the "green solvent" THF at different concentrations. Unlike the typical spin-coating protocol, where the solution is dropped onto the static substrate prior to spinning, the undoped Spiro film was prepared in a dynamic spin-coating method, as illustrated in Scheme 1: the Spiro solution was dropped onto a substrate consisting of the as-prepared perovskite film that was spinning at a preset rate. Dynamic spin-coating was adopted because of the high volatility of THF compared to CB. When using common spin-coating, the THF solvent evaporates quickly, and the Spiro film cannot even be formed in this way. While in the dynamic spin-coating method, the fast evaporation of THF can induce the relatively ordered molecular packing of Spiro molecules, as revealed by the GIWAX result discussed below. For comparison, the dopant-free Spiro dissolved in chlorobenzene was also prepared. To make the statements clear, Spiro-THF represents the dopant-free Spiro film prepared from THF, and Spiro-CB denotes that prepared from chlorobenzene.

Surface morphologies of perovskite films with and without the dopant-free Spiro prepared from different solvents on top are shown in **Figure 1**. The neat perovskite film shows a rough surface morphology with a root-mean-square (RMS) roughness of 21.42 nm. After Spiro deposition, the RMS roughness decreased significantly to 15.05 nm (Spiro-CB) and 10.05 nm (Spiro-THF), respectively. This demonstrates that Spiro-THF forms a smoother surface on the perovskite layer compared to Spiro-CB, and such a smooth surface serves as an efficient and selective contact between perovskite and the metal electrode, which is beneficial for charge transfer at the interface.[31]

Grazing-Incidence Wide-Angle X-ray Scattering (GIWAXS) measurements were performed to study the crystallinity of the Spiro-CB and Spiro-THF films. Shown in **Figure 2**a,b, almost no significant signal is observed for the Spiro-CB film, while a weak diffraction signal in the in-plane direction is detected in the Spiro-THF film. This confirms that the crystallinity of Spiro film is influenced by the processing solvents. Compared to the amorphous Spiro-CB film, the Spiro-THF film shows a slightly ordered molecular packing, as revealed from the diffraction peaks at $q \approx 1.3$ Å in Figure 2c. Although crystallinity of the Spiro-THF film was detected, we note that the diffraction peaks are relatively weak. This means that our method leads to a semicrystalline film instead of a rough film with excessively large crystalline domains that affect film quality, which can also be supported from the surface morphology shown in Figure 1.

Hole mobility of the Spiro films were measured by the space-charge-limited-current (SCLC) method, as shown in Figure 2d. The device structure for the SCLC test is ITO/PEDOT:PSS/undoped Spiro-OMeTAD (CB or THF)/MoO_3 (10 nm)/Ag. A hole mobility of $9.39\times10^{-5}\,cm^2\,V^{-1}\,s^{-1}$ was obtained for the Spiro-CB film, with a thickness of 39.8 nm. Meanwhile, a higher hole mobility of $1.07\times10^{-4}\,cm^2\,V^{-1}\,s^{-1}$ was obtained for the Spiro-THF film, under a thickness of 35.4 nm. The high mobility of the Spiro-THF film is consistent with our expectation and the morphology analysis.

To study whether the hole extraction property of the Spiro film was affected by different solvents and processing methods, steady-state photoluminescence (PL), and time-resolved PL decays were measured (Figure S1, Supporting Information). The strong PL emission of perovskite film was quenched remarkably after spin-coating the Spiro film. Compared to Spiro-CB, the Spiro-THF film shows more fluorescence quenching. Similarly, the PL lifetime of perovskite film is greatly reduced by the Spiro film, and the Spiro-THF demonstrates faster decay

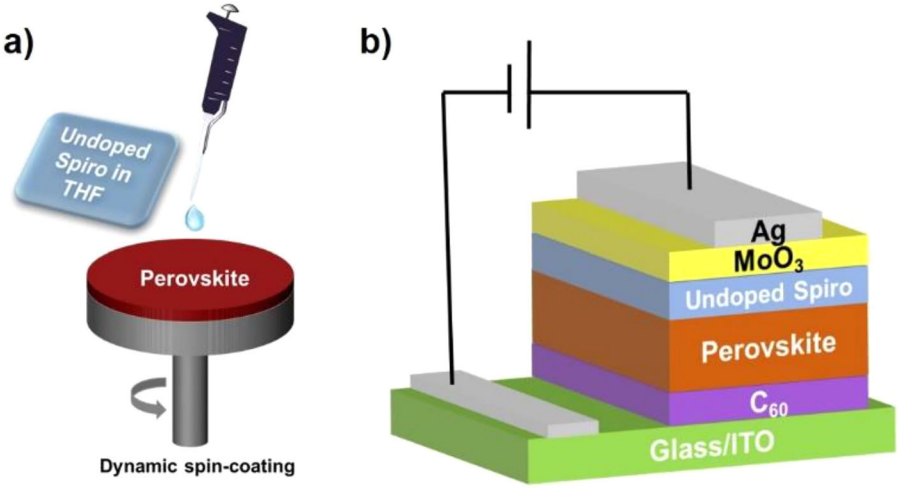

Scheme 1. a) Dynamic spin-coating of Spiro-OMeTAD dissolved in THF solution; (b) Schematic device architecture of PSCs studied.

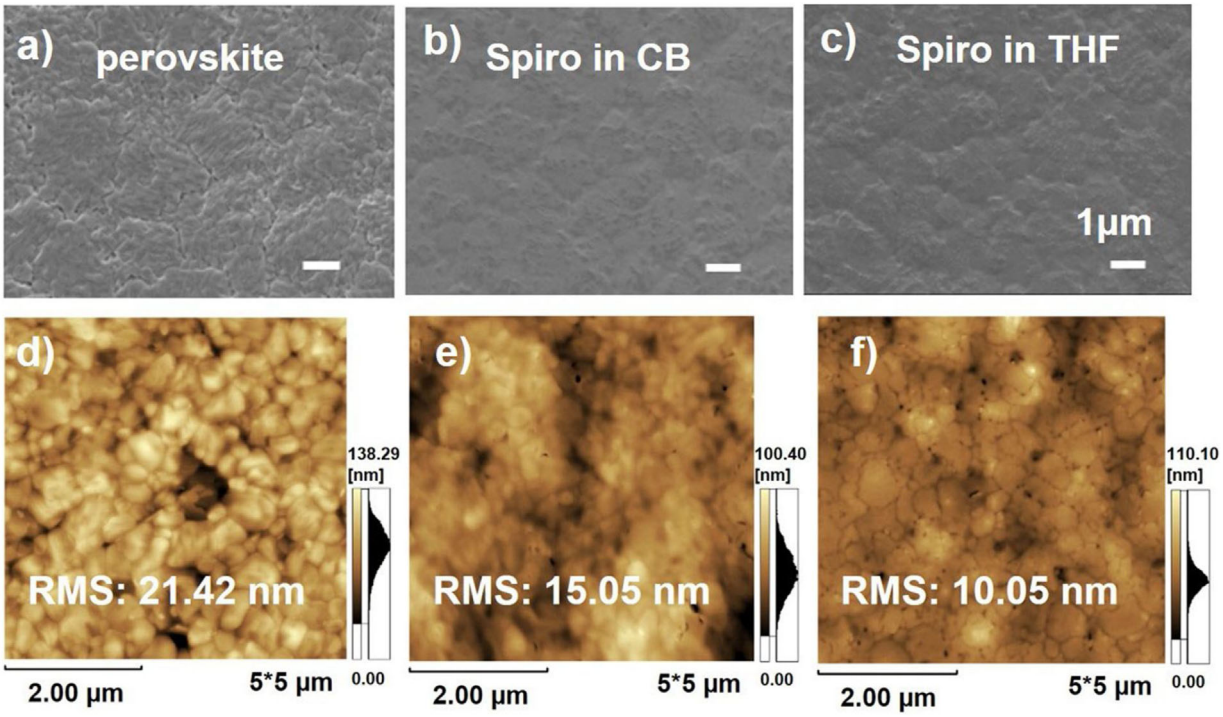

Figure 1. a–c) SEM images (the scale bar is 1 μm) and (d–f) AFM images of perovskite, perovskite/Spiro-CB, and perovskite/Spiro-THF, respectively.

than the Spiro-CB film. These results demonstrate that hole extraction from the perovskite to Spiro-THF layer is more efficient than that to the Spiro-CB layer.

To evaluate the photovoltaic performance, conventional planar perovskite solar cells were fabricated, with a device configuration depicted in Scheme 1b. Spiro films were prepared using different solvents, and their effect on device performance was evaluated. The current density-voltage (*J*-*V*) curves were recorded under 100 mW cm^{-2} AM 1.5 G solar irradiation, and the photovoltaic parameters were listed in **Table 1**. The control

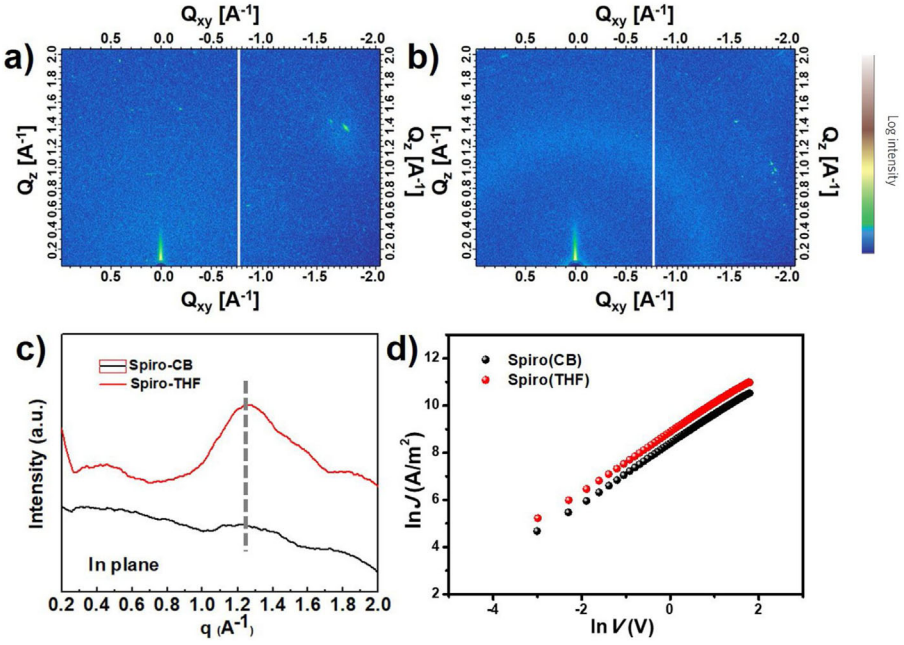

Figure 2. GIWAXS of (a) Spiro-CB and (b) Spiro-THF film; (c) GIWAXS of Spiro-CB and Spiro-THF film in the in-plane direction; (d) hole mobility tests for the Spiro-CB and Spiro-THF film.

Table 1. The photovoltaic parameters of PSCs without HTM and that with Spiro HTM prepared in CB or THF. MoO_3 represents the control device without Spiro HTM.

HTLs	V_{oc} (mV)	J_{sc} (mA cm^{-2})	*FF*	PCE (%)
MoO_3	418	7.10	28.30	0.84
Spiro-CB/MoO_3	991 (985 ± 13)	20.87 (20.70 ± 0.25)	73.83 (71.78 ± 1.76)	15.27 (14.64 ± 0.50)
Spiro-THF/MoO_3	1023 (1013 ± 13)	21.29 (21.15 ± 0.24)	77.78 (76.44 ± 1.61)	16.94 (16.37 ± 0.41)

The data in parentheses are the average values acquired from 20 devices.

device was also fabricated to verify the function of MoO_3, in which the hole transporting layer was not involved, and only a thin MoO_3 layer was evaporated on top of the perovskite layer prior to the deposition of the Ag electrode. As shown in **Figure 3**a, the control device shows a poor performance (below 1%), suggesting that the MoO_3 layer alone cannot effectively collect and transport charge carriers to the metal electrodes. In contrast, prominent enhancement in PCE is observed when the Spiro HTM is incorporated (Figure 3a). The result clearly indicates that MoO_3 here does not work as the HTM, instead, it mainly functions as a contact buffer to improve hole injection/extraction, and also protects the perovskite layer underneath, according to the previous report.[30]

Next, we varied the concentration of dopant-free Spiro in CB or THF to optimize the device performance. At a concentration of 10 mg ml^{-1}, the Spiro-CB HTM leads to maximum efficiency of 15.27%. Meanwhile, Spiro-THF at 5 mg ml^{-1} offers the optimized efficiency of 16.94%, which is superior compared with that obtained from Spiro-CB (see Table S1 and Figure S2 in the Supporting Information). Therefore, from the optimized *J-V* curves of PSCs containing dopant-free Spiro-OMeTAD, the Spiro-THF film offers higher efficiency than the Spiro-CB film. It is noteworthy that our method uses a much smaller amount of Spiro (5 mg ml^{-1}) than the conventional way (doped Spiro, 70 mg ml^{-1} is usually required).[23–24] Moreover, the dopant-free Spiro does not need to undergo the oxidation process, which reduces the processing time of the devices, that is, the oxidation process, ≈16–18 h, could be avoided. The low concentration and the short processing time are factors that could considerably lower the overall device fabrication cost (and time) and thus the levelized cost of energy (LCOE). This makes our methodology valuable for the industrial production of this technology. Excitingly, in both cases, the dopant-free Spiro-CB and Spiro-THF-based planar PSCs show neglectable hysteresis, as depicted in Figure 3b and Table S2, Supporting Information.

External quantum efficiency (EQE) spectra of the optimized devices based on Spiro-CB and Spiro-THF were measured (Figure 3c), and the integrated J_{sc} values were calculated to be 20.03 mA cm^{-2} for Spiro-THF and 19.93 mA cm^{-2} for Spiro-CB, respectively, which were consistent with that obtained from the *J–V* curves. The stabilized PCE and J_{sc} of the devices based on dopant-free Spiro-THF were evaluated at the maximum

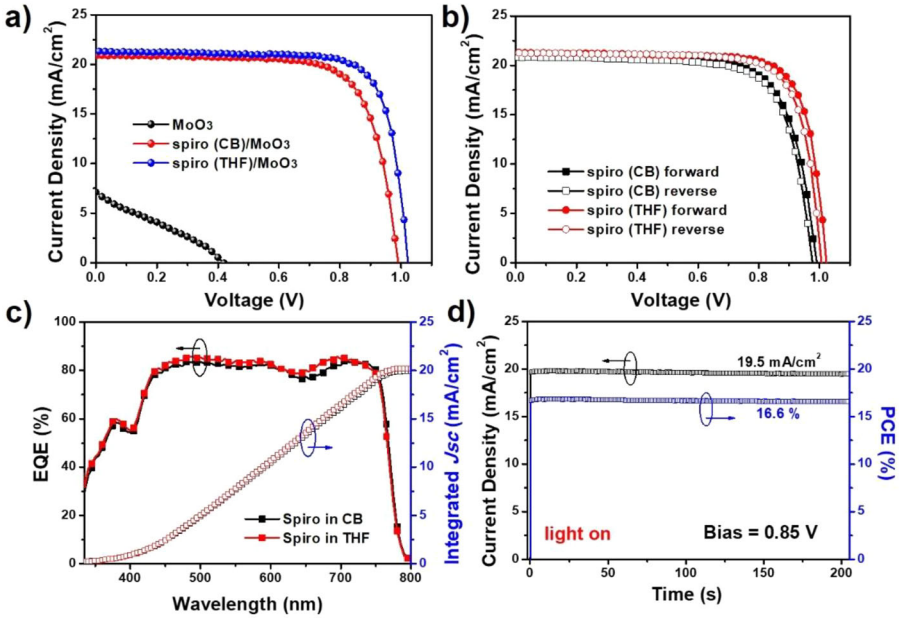

Figure 3. a) *J–V* curves of PSCs containing MoO3 buffer layer only, and that with Spiro HTM prepared in different solution; (b) Forward and reverse scanning of Spiro-CB and Spiro-THF-based PSCs; (c) EQE spectra and integrated Jsc of devices based on Spiro-CB and Spiro-THF; (d) MPP curves of the champion cell based on Spiro-THF.

power point (MPP). A stabilized efficiency of 16.6% and a current density of 19.5 mA cm^{-2} were obtained when measured at a bias voltage of 0.85 V. We are glad to note that upon illumination, both PCE and J_{sc} show an instant increase almost without time delay, confirming little hysteresis effect in the device **Figure 4**.

From the photovoltaic data summarized in Table 1, the improved efficiency in Spiro-THF-based PSCs mainly comes from the increase in FF, and also slight increases in J_{sc} and V_{oc}. According to PL experiments, Spiro-THF shows a more efficient hole extraction ability compared to Spiro-CB film. Together with its higher hole mobility, Spiro-THF shows more efficient hole transport, and thus a higher FF value. The decent hole mobility, as well as hole extraction ability, also contribute to the enhanced J_{sc} in Spiro-THF-based PSCs compared to the Spiro-CB-based one. On the other hand, Ultraviolet Photoelectron Spectroscopy (UPS) was performed to measure the work function of Spiro-THF and Spiro-CB films. According to the UPS results (Figure S3, Supporting Information), the HOMO level of Spiro-THF film is slightly lower than that of the Spiro-CB film by 0.07 eV, well supporting the slightly higher V_{oc} value in the Spiro-THF-based devices.

To compare the charge transport properties of Spiro-THF and Spiro-CB, electrochemical impedance spectroscopy (EIS) was performed. As shown in Figure S4, Supporting Information, EIS was measured at an applied voltage of 0.90 V under dark, with an equivalent circuit model consisting of a series resistance (Rs) and a recombination resistance (Rrec) at the ETL/perovskite interface. Apparently, Spiro-THF-based device exhibits a larger Rrec relative to that of Spiro-CB-based device, indicating the more reduced recombination rate occurred in the Spiro-THF -based device, which is consistent with the photovoltaic performances.

Another advantage of the dopant-free Spiro HTM is that the exclusion of the hygroscopic dopants (Li-TFSI+*t*BP) can improve the hydrophobicity of the hole transporting layer. To this end, water contact angles of Spiro films with and without dopants were measured, and the undoped Spiro-THF film shows a larger contact angle (94°) than the doped Spiro film (79°).

Consequently, PSCs using undoped Spiro-THF film shows superior ambient stability. When stored in ambient condition (25–30% RH), more than 70% of the PCE was retained in Spiro-THF-based device for 200 h, while only less than 60% of the PCE was retained for devices based on doped Spiro. When stored in an N_2-fill glove box, the devices with undoped Spiro shows a much higher stability, only about a 10% decrease in efficiency was observed. These results demonstrate the favorable stability of the dopant-free Spiro-based PSCs. Therefore, our strategy provides beneficial outcome from multiple aspects including (i) the amount of Spiro used for device fabrication is greatly reduced; (ii) the manufacturing is simplified by the exclusion of dopants and oxidation process; and (iii) the device stability is enhanced.

In summary, we demonstrated a new methodology for preparing dopant-free Spiro-OMeTAD film by dynamic spin-coating the pristine Spiro-OMeTAD solution from the halogen-free green solvent THF, which yields a record efficiency of 17% as along with a negligible hysteresis in planar PSCs. Compared to the commonly used solvent chlorobenzene, the Spiro film prepared from THF shows better crystallinity and a higher hole mobility. Notably, the amount of Spiro required in this way is much less than that in a conventional way. Overall, the negligible hysteresis effect, the green solvent processing, the much less amount of Spiro required than the traditional PSCs with doped Spiro, and the refraining from dopants together make the conventional PSCs studied in this work cost-effective, environmentally friendly, and with enhanced stability.

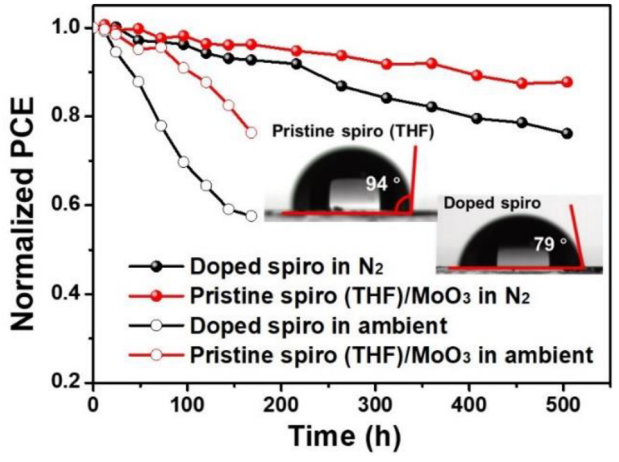

Figure 4. Photostability tests of the unencapsulated device under continuous 1 sun illumination, with doped Spiro and undoped Spiro-THF, respectively. The stability tests were conducted both in a N2-filled glove box and in ambient condition (25–30% RH). The inset presents the water contact angles of the pristine Spiro-THF film as well as the Spiro film containing dopants (Li-TFSI+tBP).

Supporting Information

Supporting Information is available from the Wiley Online Library or from the author.

Acknowledgements

K.J. and F.W. contributed equally to this work. The work was supported by the National Natural Science Foundation of China (No. 51703183), and "Project supported by Basic research and Frontier Exploration of Chongqing Municipal Science and Technology Commission (cstc2018jcyjAX0568)". We also thank HKUST President's Office for support through SSTSP project number FP201, the Shen Zhen Technology and Innovation Commission (project number JCYJ20170413173814007).

Keywords

dopant-free hole transport materials, green solvent, hysteresis, perovskite solar cells, spiro-OMeTAD

Received: December 9, 2019
Revised: February 15, 2019
Published online:

[1] A. Kojima, K. Teshima, Y. Shirai, T. Miyasaka, *J. Am. Chem. Soc.* **2009**, *131*, 6050.
[2] H.-S. Kim, C.-R. Lee, J.-H. Im, K.-B. Lee, T. Moehl, A. Marchioro, S.-J. Moon, R. Humphry-Baker, J.-H. Yum, J. E. Moser, M. Grätzel, N.-G. Park, *Sci. Rep.* **2012**, *2*, 591.
[3] M. M. Lee, J. Teuscher, T. Miyasaka, T. N. Murakami, H. J. Snaith, *Science*. **2012**, *338*, 640.
[4] H. Zhou, Q. Chen, G. Li, S. Luo, T.-b. Song, H.-S. Duan, Z. Hong, J. You, Y. Liu, Y. Yang, *Science*. **2014**, *345*, 542.
[5] W. S. Yang, B.-W. Park, E. H. Jung, N. J. Jeon, Y. C. Kim, D. U. Lee, S. S. Shin, J. Seo, E. K. Kim, J. H. Noh, S. I. Seok, *Science*. **2017**, *356*, 1376.
[6] N. J. Jeon, H. Na, E. H. Jung, T.-Y. Yang, Y. G. Lee, G. Kim, H.-W. Shin, S. Il Seok, J. Lee, J. Seo, *Nat. Energy* **2018**, *3*, 682.
[7] https://www.nrel.gov/pv/assets/pdfs/pv-efficiency-chart.20181221.pdf
[8] X. Li, D. Bi, C. Yi, J.-D. Décoppet, J. Luo, S. M. Zakeeruddin, A. Hagfeldt, M. Grätzel, *Science*. **2016**, *353*, 6294.
[9] Q. Jiang, Z. Chu, P. Wang, X. Yang, H. Liu, Y. Wang, Z. Yin, J. Wu, X. Zhang, J. You, *Adv. Mater.* **2017**, *29*, 1703852.
[10] J. Liu, Y. Wu, C. Qin, X. Yang, T. Yasuda, A. Islam, K. Zhang, W. Peng, W. Chen, L. Han, *Energy Environ. Sci*. **2014**, *7*, 2963.
[11] Z. A. Li, Z. Zhu, C.-C. Chueh, S. B. Jo, J. Luo, S.-H. Jang, A. K. Y. Jen, *J. Am. Chem. Soc*. **2016**, *138*, 11833.
[12] F. Zhang, C. Yi, P. Wei, X. Bi, J. Luo, G. Jacopin, S. Wang, X. Li, Y. Xiao, S. M. Zakeeruddin, M. Grätzel, *Adv. Energy Mater.* **2016**, *6*, 1600401.
[13] J. Zhang, T. Zhang, L. Jiang, U. Bach, Y.-B. Cheng, *ACS Energy Lett*. **2018**, *3*, 1677.
[14] Y. Liu, Q. Chen, H.-S. Duan, H. Zhou, Y. Yang, H. Chen, S. Luo, T.-B. Song, L. Dou, Z. Hong, Y. Yang, *J. Mater. Chem. A*. **2015**, *3*, 11940.
[15] S. Paek, P. Qin, Y. Lee, K. T. Cho, P. Gao, G. Grancini, E. Oveisi, P. Gratia, K. Rakstys, S. A. Al-Muhtaseb, C. Ludwig, J. Ko, M. K. Nazeeruddin, *Adv. Mater.* **2017**, *29*, 1606555.
[16] W. Yu, J. Zhang, X. Wang, X. Liu, D. Tu, J. Zhang, X. Guo, C. Li, *Solar RRL*. **2018**, *2*, 1800048.
[17] J. Luo, J. Xia, H. Yang, L. Chen, Z. Wan, F. Han, H. A. Malik, X. Zhu, C. Jia, *Energy Environ. Sci*. **2018**, *11*.
[18] J. Lee, M. Malekshahi Byranvand, G. Kang, S. Y. Son, S. Song, G. W. Kim, T. Park, *J. Am. Chem. Soc*. **2017**, *139*, 12175.
[19] X. Sun, Q. Xue, Z. Zhu, Q. Xiao, K. Jiang, H. L. Yip, H. Yan, Z. Li, *Chem Sci*. **2018**, *9*, 2698.
[20] J. Zhang, B. Xu, L. Yang, C. Ruan, L. Wang, P. Liu, W. Zhang, N. Vlachopoulos, L. Kloo, G. Boschloo, L. Sun, A. Hagfeldt, E. M. J. Johansson, *Adv. Energy Mater.* **2018**, *8*, 1701209.
[21] X. Wang, J. Zhang, S. Yu, W. Yu, P. Fu, X. Liu, D. Tu, X. Guo, C. Li, *Angew. Chem. Int. Ed. Engl*. **2018**, *57*, 12529.
[22] X. Jiang, D. Wang, Z. Yu, W. Ma, H.-B. Li, X. Yang, F. Liu, A. Hagfeldt, L. Sun, *Adv. Energy Mater.* **2018**, 1803287.
[23] Y. Xue, Y. Wu, Y. Li, *J. Power Sources*. **2017**, *344*, 160.
[24] S. N. Habisreutinger, B. Wenger, H. J. Snaith, R. J. Nicholas, *ACS Energy Lett*. **2017**, *2*, 622.
[25] C. Yin, J. Lu, Y. Xu, Y. Yun, K. Wang, J. Li, L. Jiang, J. Sun, A. D. Scully, F. Huang, J. Zhong, J. Wang, Y.-B. Cheng, T. Qin, W. Huang, *Adv. Energy Mater.* **2018**, *8*, 1800538.
[26] Y. Zhang, Z. Zhou, F. Ji, Z. Li, G. Cui, P. Gao, E. Oveisi, M. K. Nazeeruddin, S. Pang, *Adv. Mater.* **2018**, *30*, 1707143.
[27] J. K. Kim, S. U. Chai, Y. Ji, B. Levy-Wendt, S. H. Kim, Y. Yi, T. F. Heinz, J. K. Nørskov, J. H. Park, X. Zheng, *Adv. Energy Mater.* **2018**, *8*, 1801717.
[28] N. K. Noel, S. N. Habisreutinger, B. Wenger, M. T. Klug, M. T. Hörantner, M. B. Johnston, R. J. Nicholas, D. T. Moore, H. J. Snaith, *Energy Environ. Sci*. **2017**, *10*, 145.
[29] Y. Hou, X. Du, S. Scheiner, D. P. McMeekin, Z. Wang, N. Li, M. S. Killian, H. Chen, M. Richter, I. Levchuk, N. Schrenker, E. Spiecker, T. Stubhan, N. A. Luechinger, A. Hirsch, P. Schmuki, H.-P. Steinrück, R. H. Fink, M. Halik, H. J. Snaith, C. J. Brabec, *Science*. **2017**, *358*, 1192.
[30] Y. Liu, Z. Hong, Q. Chen, H. Chen, W. H. Chang, Y. M. Yang, T. B. Song, Y. Yang, *Adv. Mater.* **2016**, *28*, 440.
[31] J. Zhang, B. Xu, L. Yang, A. Mingorance, C. Ruan, Y. Hua, L. Wang, N. Vlachopoulos, M. Lira-Cantú, G. Boschloo, A. Hagfeldt, L. Sun, E. M. J. Johansson, *Adv. Energy Mater.* **2017**, *7*, 1602736.